ARTICLE

Check for updates

NiFeO$_x$ decorated Ge-hematite/perovskite for an efficient water splitting system

Ki-Yong Yoon[1], Juhyung Park[1], Minsu Jung [2], Sang-Geun Ji[1], Hosik Lee[1], Ji Hui Seo[1], Myung-Jun Kwak[1], Sang Il Seok [1], Jun Hee Lee [1] & Ji-Hyun Jang[1✉]

To boost the photoelectrochemical water oxidation performance of hematite photoanodes, high temperature annealing has been widely applied to enhance crystallinity, to improve the interface between the hematite-substrate interface, and to introduce tin-dopants from the substrate. However, when using additional dopants, the interaction between the unintentional tin and intentional dopant is poorly understood. Here, using germanium, we investigate how tin diffusion affects overall photoelectrochemical performance in germanium:tin co-doped systems. After revealing that germanium is a better dopant than tin, we develop a facile germanium-doping method which suppresses tin diffusion from the fluorine doped tin oxide substrate, significantly improving hematite performance. The NiFeO$_x$@Ge-PH photoanode shows a photocurrent density of 4.6 mA cm^{-2} at 1.23 V$_{RHE}$ with a low turn-on voltage. After combining with a perovskite solar cell, our tandem system achieves 4.8% solar-to-hydrogen conversion efficiency (3.9 mA cm^{-2} in NiFeO$_x$@Ge-PH/perovskite solar water splitting system). Our work provides important insights on a promising diagnostic tool for future co-doping system design.

[1] School of Energy and Chemical Engineering, Department of Energy Engineering, Ulsan National Institute of Science and Technology (UNIST), Ulsan, Republic of Korea. [2] School of Chemical and Environmental Engineering, Dong-Eui University, Busan, Republic of Korea. ✉email: clau@unist.ac.kr

Hematite (α-Fe₂O₃) is considered a promising material for photoelectrochemical water splitting because of its suitable band gap (2.0–2.2 eV), low cost, natural abundance, and good stability in alkaline environments[1–6]. However, hematite features a short hole-diffusion-length (>5 nm)[7–9], low electrical conductivity[10–12], and low absorption coefficient issues[1,13,14]. For these reasons, hematite has shown poor oxygen evolution activity as a photoanode, which is strongly related to a high recombination-rate[15–17]. It thus has a substantially lower solar-to-hydrogen (STH) conversion efficiency than the theoretical value (~15%). Doping to improve the poor charge transfer behavior is one of the most powerful strategies that has been suggested to address these notable drawbacks[10,18–25]. But even when Si[22,23,26,27], Sn[18,19,28–30] and Ti[20,21,31–36] atoms were broadly utilized as representative dopants, the hematite photoanode doped with these heteroatoms still exhibited low conversion efficiency.

Therefore, seeking alternative dopants may provide a more straightforward way of overcoming hematite's low conversion efficiency. Among various dopant candidates[37–39], germanium (Ge) may be the most promising alternative as an n-type dopant[37]. Ge can dramatically enhance donor density while maintaining the crystallinity of hematite, leading to an outstanding solubility in hematite[37,40]. Prezhdo et al. reported density functional theory (DFT) calculation results showing that Ge was more soluble in hematite than Si and Sn due to the balance between atomic radius and formation enthalpy[37]. Further, Ge has a guiding effect on the preferential growth of the (110) plane of the hematite crystal, which promotes high electrical conductivity[40,41].

Despite theoretical results that Ge could provide the superior photoelectrochemical properties compared with the current representative dopants in various respects, the highest water splitting performance for Ge-doped hematite reported so far is still far lower than those for representative dopants-doped hematite[18,23,31,40]. The strong discrepancy between calculated results and experimental data for doped hematite may be attributed to some variables that were neglected in the calculation. We hypothesized that unintentional Sn-doping from the fluorine-doped tin oxide (FTO) substrate, which inevitably occurs during the high-temperature annealing process (above 700 °C) is one of such variables. It has been proved that thermal diffusion of Sn from the FTO substrate indeed occurs and it is one of key factors which boosts PEC performance[18,42–44]. Like this, Sn doping from the FTO substrate is known to improve the crystallinity of hematite or the presence of diffused Sn was often ignored in heteroatom-doped systems. Therefore, for a more realistic experimental approach, the presence of the Sn dopant and its specific impact need to be carefully considered in relation with the desired dopant.

Here we report that the water splitting performance of Ge-doped porous hematite (Ge-PH) can bring the experimental data more closely in line with the superior theoretical results of Ge-doped hematite by preventing the unintentional Sn-doping. The approach produces a remarkable performance improvement compared to previous Ge-doped hematite (Ge-H), as well as hematite prepared with the commonly used representative dopants (Ti, Sn, and Si).

We confirmed by both experiment and DFT calculation that when the Ge and Sn dopants were co-present, the crystallinity of the hematite significantly deteriorated due to structural distortion. We also proved that Ge-doping by the thermal diffusion of Ge in the GeO₂ overlayer, reported in this study, mitigated the Sn diffusion into the hematite lattice and created numerous OER active sites, while maintaining the crystallinity of the hematite surface. More importantly, we report that Ge-PH can lower the overpotential of OER than pure hematite, using both theoretical simulations and experimental data.

With these synergies, our Ge-PH with NiFeOₓ co-catalyst (NiFeOₓ@Ge-PH) exhibited a photocurrent density of 4.6 mA cm⁻² at 1.23 V$_{RHE}$, achieving around a 460% enhancement in PEC performance compared with undoped hematite (~1.0 mA cm⁻² at 1.23 V$_{RHE}$).

By coupling a perovskite solar cell (PSC) to the back of our photoanode, we achieved ca. 4.8% SHT efficiency for a tandem PEC water splitting system. Our Ge-PH effectively maximized the efficiency of a solar water splitting, supported by a low turn-on voltage system with high performance.

To the best of our knowledge, this work demonstrates the highest STH efficiency for a single hematite photoanode-based tandem device, which may be a stepping-stone for a breakthrough in stagnant hematite-based PEC performance.

Results and discussion
Fabrication process and morphology effect
Fabrication process of Fe₂O₃, Ge-H, and Ge-PH. Pristine α-Fe₂O₃ (Fe₂O₃) and Ge-doped Fe₂O₃ (Ge-H) photoanodes were fabricated using conventional methods as reported (Fig. 1a)[40,41,45]. Briefly, β-FeOOH nanorods were grown on an FTO substrate using the common hydrothermal method and then rapidly annealed at 800 °C for 20 min to form Fe₂O₃ (top in Fig. 1a). Ge-H (bottom in Fig. 1a) refers to bulk Ge-doped Fe₂O₃ hydrothermally grown in a mixture solution of FeCl₃ and GeO₂ followed by a rapid annealing step at 800 °C for 20 min as reported previously[5,31]. To fabricate the Ge-PH (middle in Fig. 1a), as-fabricated β-FeOOH nanorods were immersed in a Ge solution for 30 min and rapidly annealed. The Ge solution for doping was made by dissolving GeO₂ powers in deionized water. Since all of the samples were subjected to the high-temperature annealing step (800 °C for 20 min), which creates Sn-doped Fe₂O₃, we deliberately omit mentioning the Sn for simplicity in this study.

Morphology of Fe₂O₃, Ge-H, and Ge-PH. Figure 1b–d is SEM and TEM images of the as-prepared hematite photoanodes, verifying morphology can be controlled simply by the surface treatment of the β-FeOOH nanorods. Fe₂O₃ and Ge-H showed a conventional worm-like morphology with ~70 nm diameter and ~300 nm length. The Fe₂O₃ nanorods in the Fe₂O₃ and Ge-H had a thicker diameter and lower length than β-FeOOH nanorods, since the Fe₂O₃ nanorods were collapsed and coarsened during the high-temperature annealing process, as shown in Fig. 1b, c. However, in Ge-PH, the nanorods had a diameter and length (diameter: ~50 nm and length: ~350 nm) similar to β-FeOOH nanorods, but with a nanoporous structure, as shown in Fig. 1d and Supplementary Fig. 1. By applying a GeO₂ overlayer on β-FeOOH before the annealing process, nanoporous hematite was created. In brief, the pore generation mechanism in Ge-PH is as follows. (i) The immersion of β-FeOOH into the Ge solution creates a thin GeO₂ layer on the surface of the FeOOH. The thin GeO₂ layer serves as a hard template to prevent the melting of the hematite during the annealing process (Supplementary Figs. 2 and 3)[42]. (ii) The GeO₂/β-FeOOH undergoes in situ conversion into Ge-PH by subsequent high-temperature annealing. In this process, the mass evaporation of water in the hard template generated vacancies in the GeO₂/β-FeOOH. This high-temperature dehydration creates Ge-PH with mesopores inside, via the previously reported gas entrapping mechanism[5]. In addition, the Kirkendall effect, the motion of the interface between two materials due to different diffusion rates of each atom, was partly involved in the creation of pores, as reported by Gong's group[46]. Due to the low density of the active material, Ge-PH is more transparent than Fe₂O₃ and Ge-H (Supplementary Fig. 4).
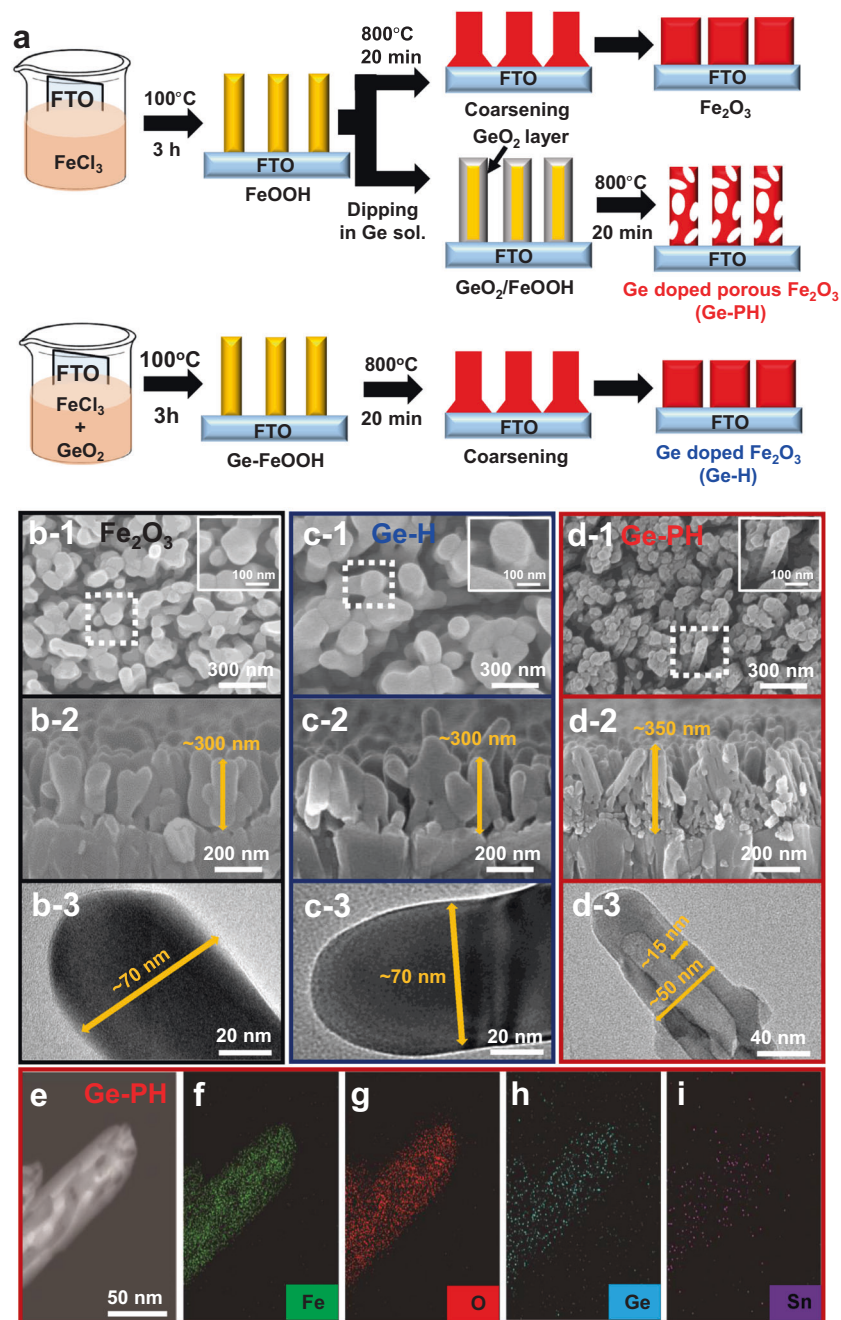
Fig. 1 Fabrication process and morphology of Ge-PH. a Scheme for fabrication of the Fe$_2$O$_3$, Ge-H, Ge-PH. **b** Scanning electron microscopy (SEM) and transmission electron microscopy (TEM) images (top-view (b-1, c-1 and d-1), cross-section (b-2, c-2 and d-2) and TEM image (b-3, c-3 and d-3)) of **b** Fe$_2$O$_3$, **c** Ge-H and **d** Ge-PH. **e** Scanning transmission electron microscopy (STEM) image of Ge-PH and the corresponding elemental mapping of **f** Fe, **g** O, **h** Ge and **i** Sn.

As shown in Fig. 1e–i, the energy dispersive X-ray (EDX) mapping of Fe, O, Ge and Sn elements by STEM analysis shows spatially uniform distribution and the porous morphology of the Ge-PH.

Ge-PH with a nanoporous structure has two main advantages over Fe$_2$O$_3$ or Ge-H. First, the path distance for the generated holes to travel from inside to the surface of the hematite, where oxygen generation occurs, is shortened (10–15 nm), which helps address the critical issues of the short hole-diffusion length of hematite, as shown in Fig. 1d. We compared the PEC performance of the samples with front and back illumination, which confirmed that Ge-PH had the shorter diffusion length for

holes to reach the surface as shown in Supplementary Fig. 5. Second, the occurrence of pores in the Ge-PH increases the number of reaction sites for oxygen evolution, simply by increasing the surface area. As shown in the BET data for the surface area and pore distributions (Supplementary Figs. 6 and 7), Ge-PH exhibited five-fold (~10 m^3/g) increased surface area compared to Fe$_2$O$_3$ or Ge-H (~2 m^3/g) with a mesopore morphology. Besides the structural differences between Ge-H and Ge-PH, the Ge in Ge-PH was doped in the final step by the thermal diffusion of Ge from the surface, whereas the Ge was uniformly doped in Ge-H at the beginning step, during the process of forming the β-FeOOH state.
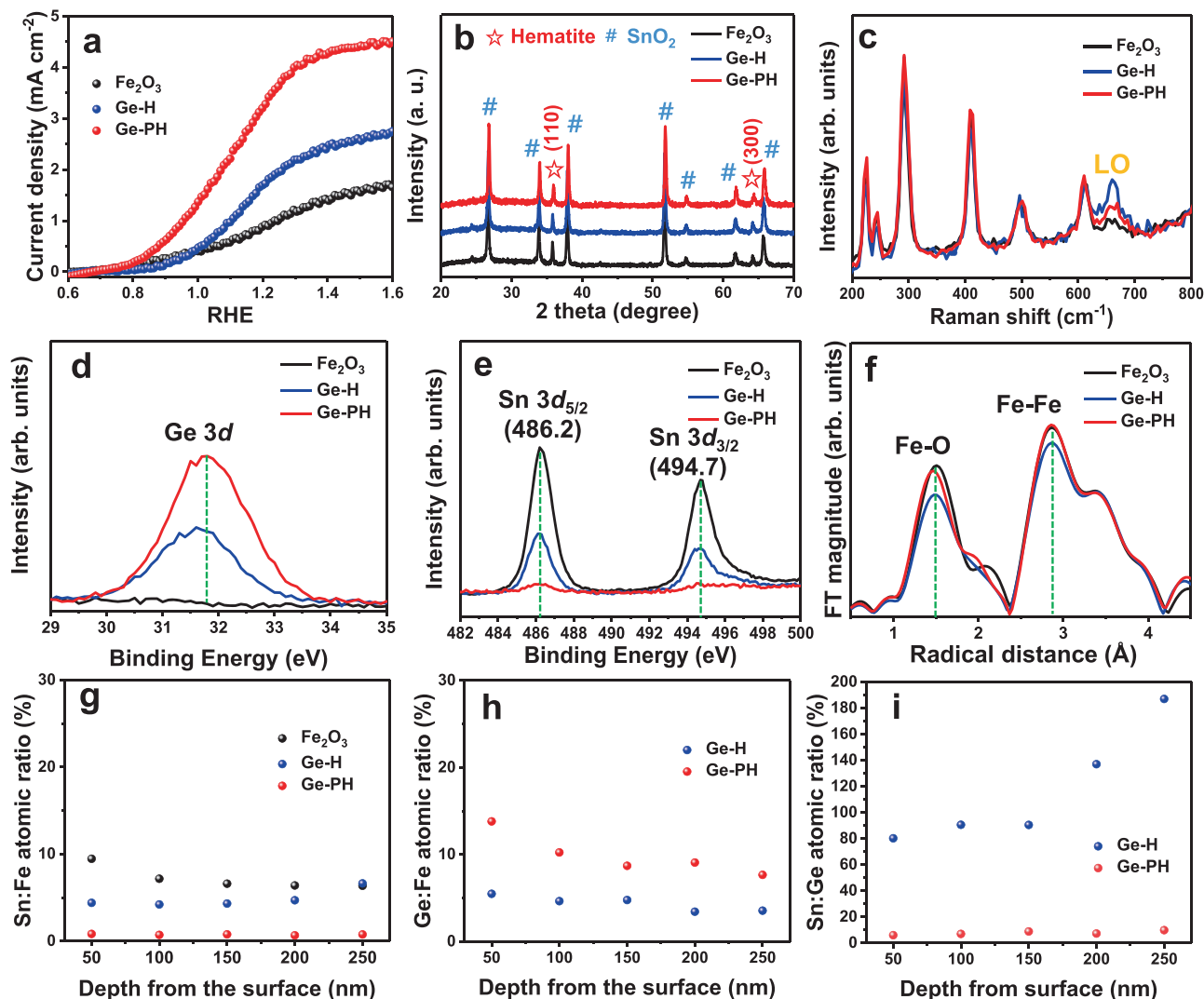
Fig. 2 The performance and structure analysis of various photoanodes. a Comparison of the photoelectrochemical performance of Fe_2O_3, Ge-H, and Ge-PH in a 1 M NaOH (pH = 13.6) electrolyte under simulated sunlight illumination (1 SUN). **b** Comparison of b) XRD patterns and **c** Raman spectra of Fe_2O_3, Ge-H, and Ge-PH. XPS spectra of **d** Ge 3d, and **e** Sn 3d. **f** Fourier transform of the EXAFS data at the Fe k-edge of the hematite nanostructures in Fe_2O_3, Ge-H, and Ge-PH. The XPS depth profiles of **g** Sn, **h** Ge, and **i** calculated Sn:Ge doping ratio.

PEC water oxidation activity and characterization. Figure 2a compares the photocurrent density generated from samples prepared with different doping methods during the photoelectrochemical water-splitting process. The Ge-PH photoanode delivered around 3.5 times (~3.5 mA cm^{-2} at 1.23V$_{RHE}$) and 1.8 times higher photocurrent density compared to the Fe_2O_3 (~1.0 mA cm^{-2} at 1.23V$_{RHE}$) and Ge-H (~1.9 mA cm^{-2} at 1.23V$_{RHE}$) photoanodes, respectively.

To determine whether this remarkable improvement was simply due to the hematite porosity, we fabricated Fe_2O_3 with a similar porous morphology using other currently representative dopants (Sn, Ti, or Si). The results clearly showed that Ge was superior to Sn, Ti or Si dopants for hematite, as shown in Supplementary Fig. 8.

The reason can be explained by the advantage of Ge as a dopant in hematite, including the feasible atomic radius of Ge, and the low formation enthalpy of the secondary phase of GeO_2 as previously reported[27].

In particular, Ge-PH showed high performance at low voltage without an anodic shift in the onset potential, despite the doping. It has been reported that, in a typical doping system, the increase in defect sites produced by doping can enhance carrier mobility,

and carrier density in the bulk, while simultaneously providing recombination sites on the surface, resulting in an anodic shift of the onset potential[47]. Furthermore, the Fe^{2+} formed by n-doping in hematite is also known to act as a recombination site on the surface, which consequently retards the water oxidation reaction in doped hematite[48]. This is in accordance with the anodic shift of the onset potential for all doped hematite photoanodes (Sn, Ti, Si-doped hematite), including the Ge-H in this study, compared to that for Fe_2O_3. Therefore, one of the critical issues has been to optimize the two components (onset potential vs current density), which operate in an opposite manner at 1.23V$_{RHE}$.

Thus, the result here that the Ge-doping in Ge-PH did show a cathodic shift of the onset potential is certainly interesting (Supplementary Fig. 9), and suggests that there could be an important factor in our Ge-PH (Surface Ge-doped hematite).

To explore this phenomenon more systematically, we carried out various scientific analyses of Ge-H and Ge-PH. First, the XRD patterns showed similar hematite peaks to Fe_2O_3 without the new phase formation in Ge-H and Ge-PH, as shown in Fig. 2b. In the Raman spectra, the appearance of the forbidden longitudinal optical (LO) mode, corresponding to the peak at 660 cm^{-1}, is indicative of the symmetry breakdown induced by structural

disorder, scattered LO phonons[4]. The LO peak was largely increased and broadened in the Ge-H, compared to Fe_2O_3, whereas the much reduced LO peak was observed in Ge-PH, as shown in Fig. 2c. This implies the symmetry breaking by Ge-doping in Ge-H is much larger than in Ge-PH.

A correlation between the Ge and Sn dopants was confirmed by X-ray photoelectron spectroscopy (XPS) data. The observation of a Ge 3d peak at ~31.6 eV from Ge-PH indicates that the Ge atoms were successfully doped in Fe_2O_3 with a higher content of Ge compared to Ge-H by the high-temperature annealing process, as shown in Fig. 2d and Supplementary Fig. 10[41,45].

The Sn 3d peaks centered at 494.7 (Sn $3d_{3/2}$) and 486.2 eV (Sn $3d_{5/2}$) of Fe_2O_3, Ge-H, and Ge-PH in Fig. 2e suggest that all of the hematite samples were unintentionally doped by Sn^{4+} ions from the FTO substrate during the high-temperature annealing process[18,42]. It should be noted that the Ge-PH had much a lower Sn dopant content than Fe_2O_3 and Ge-H. This can be attributed to the GeO_2 overlayer and the relatively long and thin nanorod morphology of Ge-PH, as compared with the coarsened short and bare nanorods of Fe_2O_3 and Ge-H, as shown in Supplementary Fig. 3[42]. The thinner and longer nanorods of the Ge-PH have lower chances of bulk Sn diffusion from the bottom FTO substrate during the high-temperature annealing process. In addition, the GeO_2 overlayer can suppress surface Sn diffusion from the surrounding area of the nanorods on the FTO substrate.

In order to check the effect of Sn content on the crystallinity of the doped sample, we carried out extended X-ray absorption fine structure (EXAFS) measurements, which also included information about the inter-atomic distance and the local dynamics of the system. X-ray absorption near edge structure (XANES) results which show the oxidation state change of the host atom can be found in Supplementary Fig. 11. The Fourier transform of the EXAFS results in the R space in Fig. 2f shows a clear difference among the three samples with different doping conditions. The peak around 1.5 Å and 3 Å can be attributed to Fe–O bonds and Fe–Fe bonds, respectively. The decreased intensity of the Fe–O and Fe–Fe bonding lengths for Ge-H compared to Fe_2O_3 was confirmed, revealing there was a prominent distortion of the crystal structure after Ge doping. Also, an increased R space was observed for the Fe–O bonding length in Fe_2O_3 and Ge-H, indicating the formation of a lower oxidation state of Fe, such as Fe^{2+}.

We hypothesized that these probably suggest that Sn has a greater influence on structural distortion, due to the larger atomic size than Fe and the excess charge coming from the n-type dopants[49].

To clearly pinpoint these assumptions, the chemical compositions of Fe_2O_3, Ge-H, and Ge-PH were examined by XPS depth profile. The results showed that the Sn-doping ratio of Fe_2O_3 and Ge-H were 4.5–9.5% in the whole region. However, the doping ratio of Sn in Ge-PH was much reduced, with a maximum 0.7–0.8% in the whole region as shown in Fig. 2g. This suggests that unintentional Sn-doping by thermal diffusion from the FTO substrate was suppressed by the GeO_2 overlayer in the long and thin nanorods compared to the short and thick nanorods without the overlayer. Since Ge-PH has an unfavorable and long Sn diffusion path from the bottom FTO substrate, it has less Sn content on the surface of the hematite where the OER reaction occurs, resulting in fewer chances for Ge:Sn combination, as described in Fig. 3e.

The Ge-doping ratios of Ge-H and Ge-PH were measured to be 3.4–5.5% and 7.7–13.8% in the whole structure region, as shown in Fig. 2h. Although the total doping content (Sn + Ge) of Ge-H and Ge-PH was similar (around 8–14%, Supplementary Figs. 12 and 13), the doping ratio (Sn/Ge) of Ge-H was 14–19 times higher than in Ge-PH. Therefore, we can conclude that when the

content of Sn increases significantly, it will have a negative effect that causes structural distortion (as proven in Fig. 2c, f). The lower content of Sn:Ge in the surface region of Ge-PH, which was clearly observed in the XPS depth profile, well explains the cathodic shift of the onset potential, indicating reduced recombination in the OER reaction. We checked the content of the oxygen vacancy in each sample because it can promote the reaction kinetic and increase the carrier density to enhance the charge transfer and suppress recombination. Ge-PH showed the highest oxygen vacancy content as shown in Supplementary Fig. 14. Since the oxygen vacancy content increases with an increasing doping concentration and Ge is easily diffused from the surface GeO_2 layer, the oxygen vacancy of Ge-PH was high but still within the oxygen vacancy level of typical Fe_2O_3[50]. As can be seen in Supplementary Fig. 14b, all samples showed similar OER curves in dark conditions which indicate that the level of the oxygen vacancy contained in our samples did not cause a change in the OER mechanism.

Theoretical and experimental investigation on the effect of Ge: Sn co-doping

Solubility of Sn and Ge in hematite. To understand the solubility of Sn and Ge in hematite, we calculated the formation energy for Sn-doped Fe_2O_3, Ge-doped Fe_2O_3, and Ge:Sn co-doped Fe_2O_3, as shown in Fig. 3a. The formation energy for Ge:Sn co-doping (blue) and Sn-doping (pink) was higher than that for Ge-doping (red). The high formation energy of Ge:Sn co-doping in Fe_2O_3 specifically indicates the low dopant solubility and low ionization of the Ge dopant in hematite[37]. We explored the structure distortion caused by the presence of Ge and Sn by comparing the atomic structures of Ge-doped hematite and Ge:Sn co-doped hematite using DFT calculations. As can be seen in Fig. 3b, the Ge:Sn co-doped hematite experiences greater symmetry breaking after the re-positioning of the Fe atoms, while the substitutional single Ge-doping did not produce any noticeable distortion in the atomic arrangement.

Based on DFT calculations, we drew the atomic arrangement of hematite with the substitution of heteroatoms to clearly understand this phenomenon, as shown in Fig. 3c. Single-Ge-doped hematite did not show much distortion since the Ge dopant has a radius similar to Fe in hematite, and Ge becomes more soluble than other representative metal dopants. In the case of Sn-doped hematite, relatively high structural distortion occurs since the Sn dopant has a larger radius than Fe. When Ge and Sn are co-present, additional strong electron repulsion between Fe atoms neighboring the Ge and Sn dopants is produced by the excess electron charges from the n-type metal dopants in Fe_2O_3. FTO is preferentially used as a substrate of hematite-based photoelectrodes, since it withstands the high temperatures for hematite activation (>700 ºC) relatively well compared to other transparent substrates, including AZO or ITO[43,51,52].

Observation of the structural disorder. Figure 3d is the XPS spectra of Fe 2_p, which shows that Ge-H has more Fe^{2+} than Ge-PH. A structural strain can occur due to a mismatch in the atomic radius upon doping. Sn has a very large radius compared to Fe, whereas the Ge atom has a similar radius to the Fe atom. Since Fe_2O_3 and Ge-H have more Sn content compared to Ge-PH, a higher content of Fe(II) was observed as shown in Fig. 2g. Ge-H has a large amount of diffused Sn, where Ge is present throughout the hematite nanorod. In Ge-PH, however, the majority of the Ge and Sn dopants are positioned in different regions, and the amount of diffused Sn is relatively small in the surface region where the OER reaction occurs specifically, thus minimizing the adverse effect caused by the co-existence of the two n-dopants, as shown in
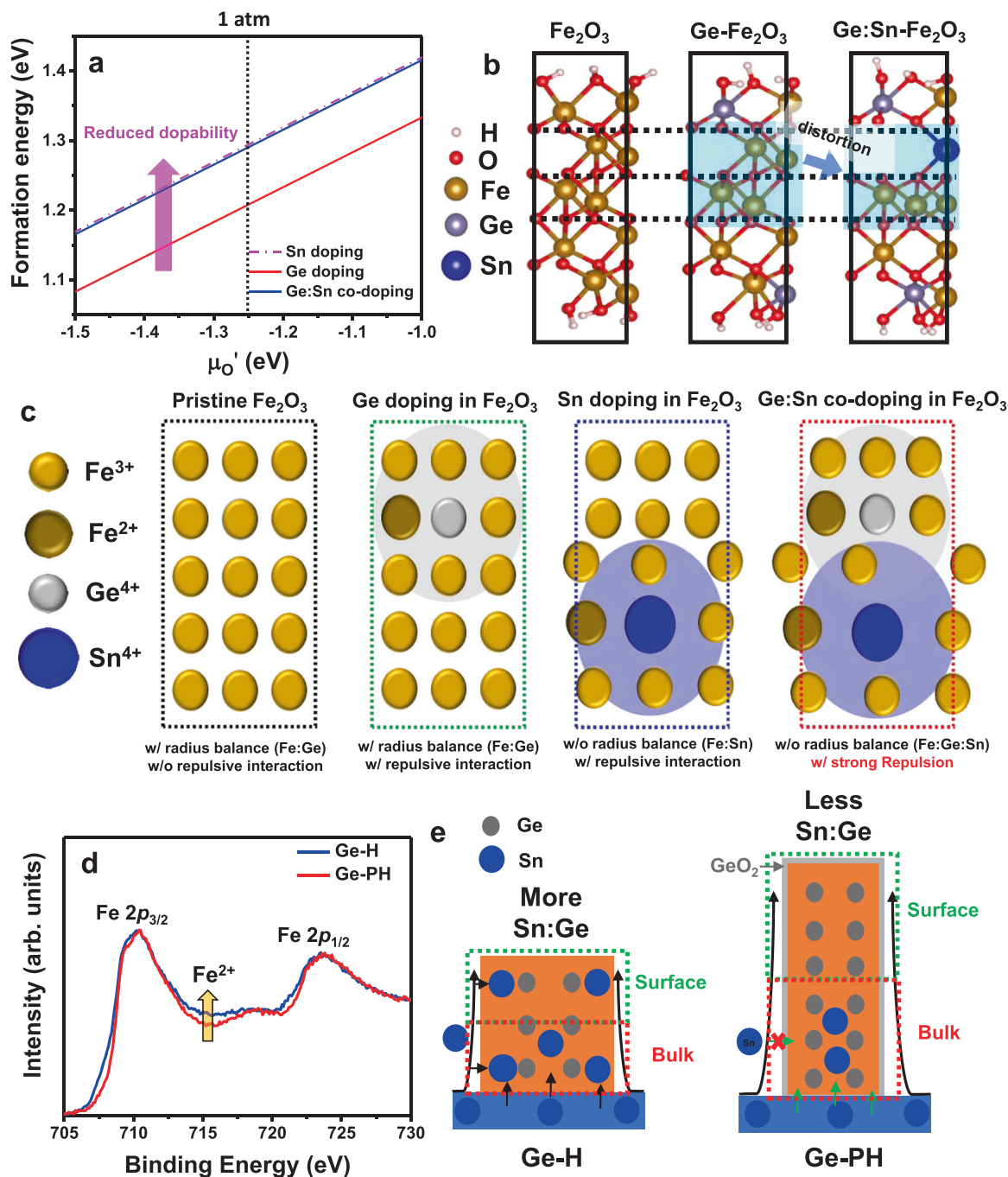
Fig. 3 DFT calculations and experimental results for Ge and Sn interaction. a The formation energy for Sn-doping, Ge-doping, and Ge:Sn co-doping in Fe_2O_3. The dotted line represents 1 atm at which the experiments were performed. **b** DFT calculations of atomic arrangements of Fe_2O_3 with different dopant environments. **c** Atomic structure of Ge-doped Fe_2O_3 Sn-doped Fe_2O_3 and Ge:Sn co-doped Fe_2O_3. **d** XPS spectra of Fe 2_p. **e** Schematics of the distribution of Sn and Ge according to co-doping methods.

Fig. 3e. Therefore, due to the lower content of Sn, Ge-PH was expected to experience a lesser distortion than Ge-PH.

These results well explain the XRD, Raman, EXAFS, XPS spectra, onset potential, and the PEC activity observed in Fig. 2 and Supplementary Fig. 9, which show that the structural distortion observed in Ge-H caused by co-doping of Sn and Ge in hematite was almost recovered in Ge-PH, which had a status similar to the original undoped hematite.

Recombination rate and surface activity. Between the two n-type elements investigated in this study, Ge is superior to Sn,

which was confirmed by electrochemical analysis (Supplementary Fig. 15). The highest charge carrier density of Ge-PH, which is inversely proportional to the lowest slope of the curve in the Mott-Schottky plot (Fig. 4a), was in a good agreement with the simulation and experimental results. These results are consistent with the impedance data in Fig. 4b and electrical conductivity data in Supplementary Fig. 16. Therefore, enhanced carrier density and electrical conductivity of Ge-PH can maximize the PEC performance. From the Mott-Schottky plot, we also investigated the flat band potential as shown in Table 1. Basically, hematite with a low flat band potential delivers a low onset
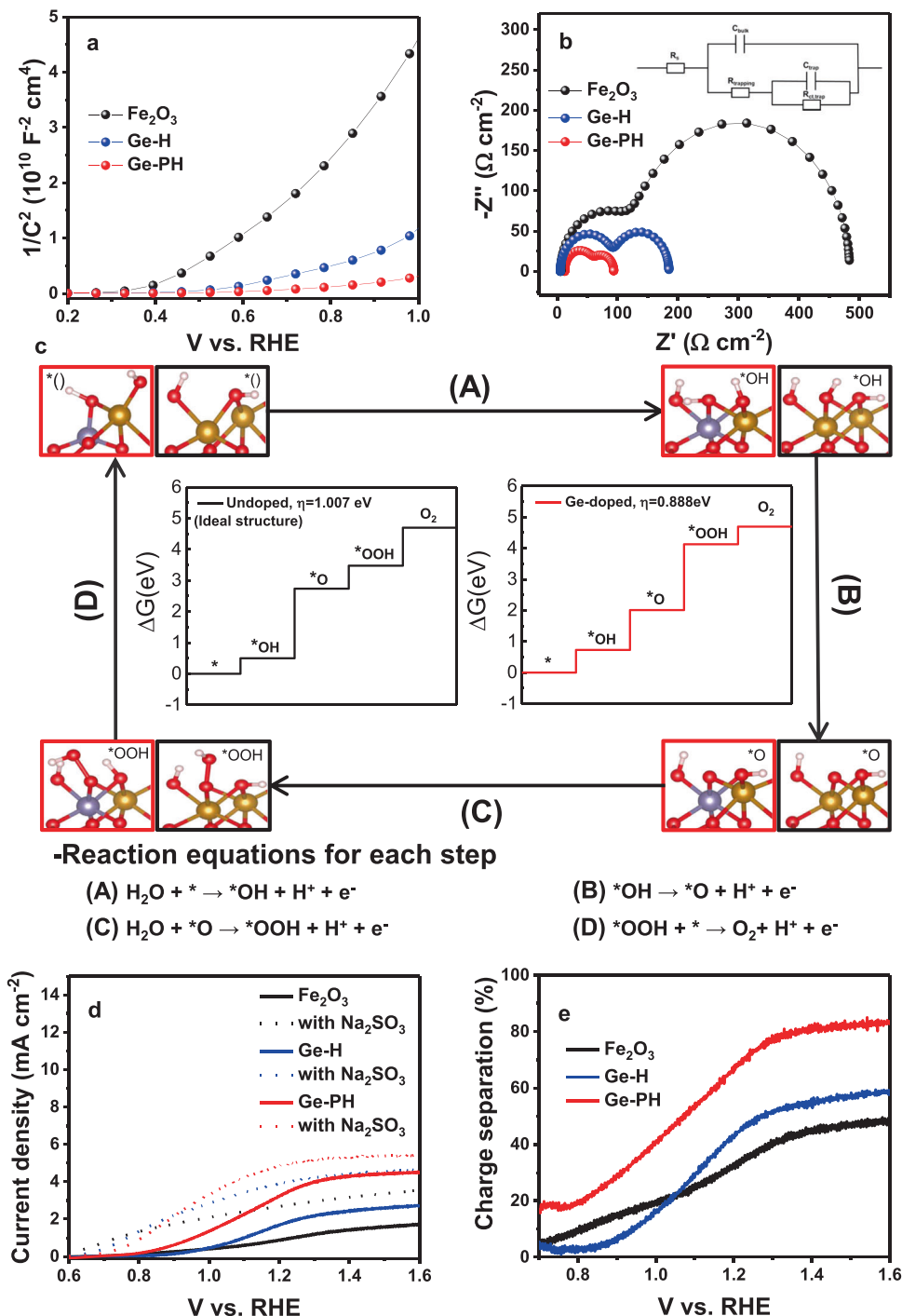
Fig. 4 Electrochemical analysis and simulated OER activity. a Mott-Schottky plots and **b** EIS measurements (with the circuit model). **c** Free energy diagrams of the intermediates on Fe_2O_3 (undoped) and $Ge-Fe_2O_3$ (Ge-doped). For comparison, the free energies of the OER species on the hematite (0001) surface from the literature are included. Brown, gray, red, and white are Fe, Ge, O, and H atoms, respectively. **d** LSV curves of Fe_2O_3, Ge-H, and Ge-PH under illumination in 1 M NaOH (solid line) and a solution mixture of 1 M NaOH and 0.5 M Na_2SO_3 (dashed lines). **e** Charge separation efficiencies.

Table 1 Representative results for the flat band potential (EFB), charge carrier concentration (ND), and space charge width (Wsc) from Mott-Schottky measurements.

	E_{FB} (V)	N_D (10^{20} cm^{-3})	W (nm)
Fe_2O_3	0.39	0.22	12.4
Ge-H	0.53	0.70	6.26
Ge-PH	0.43	3.10	2.97

potential as in the previously reported work[53]. In our photoanodes, Fe_2O_3 showed the lowest flat band potential (0.39V_{RHE}) compared to Ge-H (0.53V_{RHE}) and Ge-PH (0.43V_{RHE}). However, the similar onset potential of Fe_2O_3 and Ge-PH was observed due to the make-up in the flat band potential by the favorable activation energy in Ge-PH.

Figure 4b shows the Nyquist plots used to investigate the influence on the electrolyte/Fe_2O_3 interface. The R_{ct} value (charge transfer resistance between the electrolyte/material, second semicircle) of Ge-PH was much smaller than that of Fe_2O_3 or

Ge-H. And R_{trap}, a resistance related to the rate of trapping holes in the surface states (first semicircle), was also smaller than that of the other photoanodes.

To support the reduced overpotential and excellent performance in Ge-PH observed in our experimental result, DFT calculations were performed to determine the theoretical overpotential. Figure 4c shows the calculated free energy for each elementary step. In our limited study, an ideal hematite structure (without unintentional Sn diffusion) was analyzed to confirm the Ge dopant effect on the theoretical OER values (undoped vs. Ge-doped). It is known that the rate-determining step for hematite is the reaction B (*OH → *O) where the deprotonation from *OH can make the charge state (*O) very unstable[54–56]. In undoped hematite, therefore, the reaction B corresponding to deprotonation from *OH has the highest free energy in the reaction pathway and the reaction potential was determined to be 2.2372 eV. The calculated overpotential for undoped hematite is 1.007 eV, which is in reasonable agreement with previous theoretical studies for (0001) hematite[54,55].

To lower the free energy for the reaction B, it is necessary to reduce the instability of *O. When Ge is doped in hematite, the charge state of *O can be more stable since an n-type dopant Ge provides the electron to oxygen[37,39,54]. Therefore, the free energy of the reaction B is significantly reduced by Ge doping. On the other hand, due to a trade-off relationship of the free energy between the reaction B (*OH → *O) and the reaction C (*O → *OOH)[54], the rate-determining step of Ge-doped hematite is the reaction C, which has a 0.119 eV lower overpotential (0.888 eV) than undoped hematite, which is in consistent with our experimental J-V curve.

Charge separation efficiency was calculated based on the LSV curves under illumination in 1 M NaOH and 1 M NaOH containing 0.5 M hole scavenger, Na_2SO_3, as shown in Fig. 4d. Notably, Ge-PH showed a substantially higher charge transfer efficiency than Fe_2O_3 and Ge-H over the entire tested potential range, and approached 80% at potentials beyond $1.3V_{RHE}$ as shown in Fig. 4e. The results of the electrochemical analysis and DFT calculations clearly support the reason for the low onset potential of Ge-PH.

$NiFeO_x$@Ge-PH/PSC solar water splitting performance. In order to confirm the feasibility of our photoanode for solar water splitting, we evaluated the performance of Ge-PH in a tandem configuration[57–61]. We prepared a tandem device containing a single PSC and a hematite photoanode similar to the Z-scheme in natural photosynthesis, in which two semiconductors with different absorption spectra are efficient over a broad part of the solar spectrum, and deliver a high STH efficiency for water splitting.

For this setup, we employed a PSC fabricated using a recently developed procedure (short-circuit current (J_{sc}) = 21.60 mA cm^{-2}, open-circuit voltage (V_{oc}) = 1.16 V, and fill factor (FF) = 75.07%; power conversion efficiency (PCE) = 18.85%, Supplementary Fig. 17)[62]. The PSC is unable to drive the reaction on its own (or with an efficient electrocatalyst) because its photovoltage is less than what is thermodynamically required to split water[58,59].

A schematic of the tandem configuration, with the PSC connected electrically and optically in series with the hematite is shown in Fig. 5a. To boost PEC performance, $NiFeO_x$, one of the representative OER catalysts used in hematite-based PEC systems, was deposited on the surface of the Ge-PH photoanode. $NiFeO_x$ can greatly reduce the recombination via a facile charge separation process by enhancing the transfer kinetics for OER. Therefore, $NiFeO_x$/Ge-PH (in water) achieved almost the same

performance as Ge-PH with a sacrificial agent (in sulfite). When $NiFeO_x$ was applied to Ge-PH, the photocurrent density of the $NiFeO_x$@Ge-PH reached 4.6 mA cm^{-2} at 1.23 V_{RHE} as shown in Fig. 5b. In addition, the $NiFeO_x$ catalyst helped shift the onset potential with enhanced performance (Supplementary Fig. 18). When $NiFeO_x$ was applied to Ge-PH, the photocurrent density of the $NiFeO_x$@Ge-PH reached 4.6 mA cm^{-2} at 1.23 V_{RHE} as shown in Fig. 5b.

To estimate the operating current density, J-V curves of the PSC were measured by placing the hematite photoanode before the solar cell to account for optical absorption by the hematite photoanode as shown in Fig. 5c. The operating current density in the tandem configuration was thus estimated to be around 3.9 mA cm^{-2}. The assembled tandem device was subsequently tested in 1 M NaOH electrolyte without additional external bias in a two-electrode configuration, using the current density versus time (J-t) curve under 1 SUN (AM 1.5 G, 100 mW cm^{-2}). The current density closely matched the operating current extracted from Fig. 5c, with good stability, as shown in Fig. 5d and Supplementary Fig. 19. The STH conversion efficiency was calculated to be 4.8% for the Ge-PH and PSC tandem systems. To the best of our knowledge, this is the highest STH efficiency obtained for a single hematite-based photoanode with a tandem device, as shown in Supplementary Tables 1–3.

Finally, we calculated the faradaic efficiency of the tandem device by measuring the H_2 and O_2 evolution under AM 1.5 illumination in 1 M NaOH electrolyte. As shown in Fig. 5e, the hydrogen gases produced on the Pt mesh and the oxygen gases on $NiFeO_x$@Ge-PH were around 68.5 and 34.0 μmol after 120 min, respectively, indicating a 2:1 ratio of the water splitting mechanism. The ratio between the measured and predicted gas evolution rates gives a faradaic efficiency of 87–95% throughout the measurements. Therefore, most of the photo-generated charges were consumed by water splitting (hydrogen/oxygen gas generation) in our tandem system.

In summary, we present an approach to achieve the theoretically potential results in a water-splitting system of co-doped hematite. We demonstrated that the morphology-controlled Ge-doped hematite with the reduced content of unintentionally doped Sn can be a stepping-stone to approach hematite's theoretical efficiency, including the high photocurrent density and the low turn-on voltage. Employing our findings and enhanced performance, the $NiFeO_x$@Ge-PH/PSC tandem system delivered the photocurrent density of ~3.9 mA cm^{-2} in 1 M NaOH electrolyte. Therefore, our insight and co-doping strategy, which reduces the Sn content in hematite for water splitting, potentially provides a paradigm for electrode design and could be further extended to other heteroatom-dopant systems (Ti, Sn, Si, Zr, and Ga) utilized in numerous applications, including solar conversion, sensing, and opto-ferroelectric devices which require doping for enhanced electrical conductivity.

Methods

Preparation of the Fe_2O_3 and Ge-doped Fe_2O_3 (Ge-H) photoanode. Bare Fe_2O_3 as a reference photoanode was grown on FTO glass utilizing aqueous chemical growth methods. The synthesis of β-FeOOH rods was performed in an aqueous solution containing 100 mL of 150 mM ferric chloride hexahydrate ($FeCl_3 \cdot 6H_2O$), and Ge-doped β-FeOOH rods was mixed with 500 μl Ge precursor. Ge precursor is completely dissolved in DI water when sonicated with 40 mM GeO_2 for 6 h to make clear solution. The solution was placed in a cap-sealed glass vial containing two back-to-back slips of FTO glass leaning against the inner wall. The glass vial was placed in a forced convection oven with a programmable temperature controller. After heating to 100 °C from 30 °C for 2 h, the temperature was maintained for 3 h, during which β-FeOOH or Ge-doped β-FeOOH rods were synthesized on the FTO substrate. The sample was thoroughly washed by water and dried by N_2 gas. The β-FeOOH rods on the FTO substrates were rapidly inserted into a furnace tube at 800 °C for 20 min and taken out to ambient conditions.
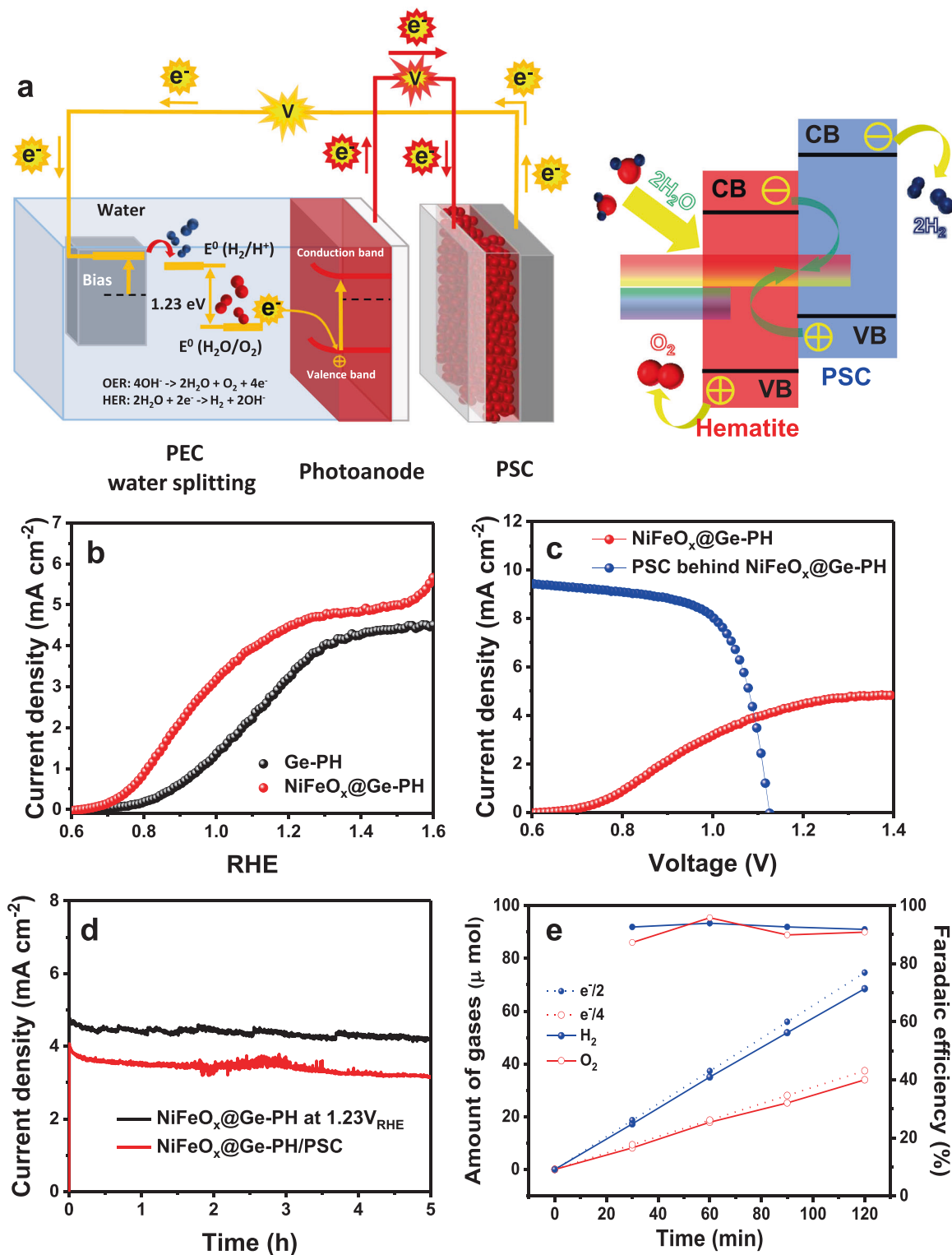
Fig. 5 NiFeO$_x$@Ge-PH/PSC solar water splitting efficiency. a Schematic of the tandem system featuring a perovskite solar cell (PSC) and photoanode with a Z-scheme of artificial photosynthesis driven by light absorption (left). Hematite was used to evolve oxygen and the PSC was used to evolve hydrogen (right). **b** J-V curves of Ge-PH and NiFeO$_x$ decorated Ge-PH. **c** J-V curves of a PSC-hematite-based photoanode tandem device together. **d** Stability of the NiFeO$_x$@Ge-PH at 1.23V$_{RHE}$ and NiFeO$_x$@Ge-PH/PSC solar water splitting. **e** Faradaic efficiency of the NiFeO$_x$@Ge-PH.

Preparation of the Ge-doped porous Fe$_2$O$_3$ (Ge-PH) photoanode. β-FeOOH grown on the FTO substrate was immersed in Ge precursor for 30 min. After washing the sample with DI water and drying by N$_2$ gas, the GeO$_2$/β-FeOOH was annealed using the same method (rapid insertion into a furnace tube at 800 ºC for 20 min and removal to ambient conditions) as was used in the preparation of Fe$_2$O$_3$ or Ge-H to create hematite with Ge-PH.

Decoration of NiFeO$_x$ oxygen evolution catalysts on Ge-PH. For depositing the NiFeO$_X$ OER catalyst on Ge-PH, the Ge-PH photoanode was immersed in a NiFeO$_x$ precursor solution. Precursor solutions were prepared from iron(III) 2-ethylhexanoate (50% w/w in mineral spirits) and nickel(II) 2 ethylhexanoate (78% w/w in 2-ethylhexanoic acid) by dissolving the appropriate amount of the metal precursor in hexanes to give a total concentration of a 15% w/w metal complex.

These solutions were further diluted with hexane to prepare a solution with a total metal concentration of 50 mM. The photoanode was irradiated with UV light (254 nm) for 1 h and was then annealed in a preheated furnace at 100 °C for 1 h.

Characterizations. The structures of the samples were characterized by SEM (Nano-SEM 230, 15 kV), TEM (JEM-2100, 200 kV), and Raman spectroscopy (WItec, alpha300R, excited by a 532 nm laser). X-ray diffraction measurements were carried out with a Rigaku Co. High power X-ray Diffractometer D/MAZX 2500 V/PC from 10º to 80º).

PEC measurements. A three-electrode configuration in a homemade photoelectrochemical kit with an exposure area of 0.09 cm² and front-side simulated AM 1.5 illumination (Sol2A class ABA 94062 A, 1000 W Xenon lamp, Newport), composed of an Ag/AgCl (KCl sat.) electrode and a Pt mesh as the reference and counter electrodes, respectively, were used for PEC measurements. The intensity of light was adjusted to 100 mW cm⁻². A 1.0 M NaOH solution was used as a pH 13.6 electrolyte. Potentials versus RHE were calculated using the Nernst equation $E_{RHE} = E_{Ag/AgCl} + 0.0591(pH) + 0.1976$ V. The scan rate for J-V curves was 20 mV s⁻¹. EIS was carried out at a frequency range from 100 kHz to 0.1 Hz using a potentiostat (VersaSTAT 3). EIS experimental data were analyzed and fitted using the Z-view software.

Methylammonium iodide (MAI) synthesis. Methylammonium iodide was synthesized by adding dropwise 57% aqueous hydriodic acid (HI, 30.0 mL) into 40% aqueous methylamine (19.6 mL) solution with vigorous stirring under an ice bath. After the addition of HI, the solution was stirred for another 2 h. The solvent was then removed under vacuum using a rotary evaporator and the precipitate was dissolved in ethanol and recrystallized in diethyl ether. The precipitates were collected by suction filtration and the resulting MAI was then dried at 60 °C under vacuum overnight. Formamidinium iodide (FAI) was also synthesized under identical conditions as described above.
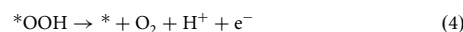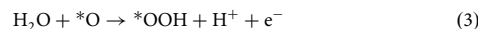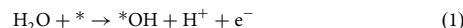
Synthesis of FAPbI₃ and MAPbBr₃ powders. Stoichiometric amounts of FAI and PbI₂ for FAPbI₃, MAI, and PbBr₂ for MAPbBr₃ were dissolved in 2-methoxyethanol under stirring at 120 °C for 30 min and 100 °C for 30 min, respectively. The precipitates were collected by suction filtration and dried under vacuum overnight.

Photovoltaic device fabrication. FTO-coated glass (Pilkington, TEC8) as a substrate was cleaned in an ultrasonic bath using detergents, acetone, and ethanol for 30 min, respectively. Titanium diisopropoxide bis(acetylacetonate) precursor solution diluted in ethanol with a ratio of 1:10 by volume was sprayed on the FTO substrate at 450 °C for coating of TiO₂ hole blocking layer (bl-TiO₂). Mesoporous TiO₂ layer (mp-TiO₂) was then deposited onto the bl-TiO₂/FTO substrate by spin-coating TiO₂ paste with an average particle size of 50 nm at 1500 rpm for 50 s. Afterwards, the substrate was annealed at 500 °C in air for 1 h. The synthesized FAPbI₃ and MAPbBr₃ powders with 8:2 mole ratio were dissolved in N-N-dimethylformamide (DMF) and dimethylsulfoxide (DMSO) with the DMF to DMSO volume ratio of 4:1 under stirring at 60 °C for 1 h. The perovskite solution filtered by PTFE syringe filter (0.2 μm) was deposited on the mp-TiO₂/bl-TiO₂/FTO substrate by two consecutive spin-coating steps at 1000 rpm for 15 s followed by 5000 rpm for 20 s with a ramping rate of 300 and 1300 rpm s⁻¹, respectively. One milliliter of ether was dropped onto the spinning substrate 10 s after starting the second spin-coating stage. The perovskite-deposited substrate was then heat-treated on a hot plate at 150 °C for 10 min. For deposition of the organic hole transporting material, 2,2′,7,7′-tetrakis-(N,N-di-4-methoxyphenylamino)-9,9′-spirobifluorene (spiro-OMeTAD) (88 mg in 1 mL of chlorobenzene) was mixed with 7.5 μL of lithium bis(trifluoromethanesulfonyl)imide (Li-TFSI) solution in acetonitrile (170 mg mL⁻¹) and 7.5 μL of 4-tert-butylpyridine (tBP). The hole-conducting material was spin-coated at 3000 rpm for 30 s on the perovskite/mp-TiO₂/bl-TiO₂/FTO. Finally, a gold layer was deposited on the hole conducting layer using a thermal evaporator.

DFT calculation details. All calculations were performed in the framework of the spin-polarized density functional theory with the projector augmented wave (PAW) method[63] using the Vienna ab-initio simulation package (VASP) code[64]. The exchange-correlation was considered using the generalized gradient approximation of Perdew, Burke, and Ernzerhof (PBE)[65]. The cut-off energy for the plane-wave basis set was 500 eV, and Monkhorst-Pack k-point mesh of $4 \times 4 \times 1$ was used for all the slab structure of α-Fe₂O₃ (hematite). The ionic positions were relaxed until a force convergence of 0.01 eV A⁻¹ was reached. Because of the strongly correlated 3d states in transition metal oxide systems, we used the GGA + U framework to modify the self-interaction[66]. The values of U-J of all the 3d metals were set to 4.2 eV for good agreement with the experimental band-gap of α-Fe₂O₃ (2.2 eV). The hexagonal unit cell of α-Fe₂O₃ was optimized with a layered anti-ferromagnetic (AFM) ordering. For pure α-Fe₂O₃ unit cell, the lattice parameters calculated within PBE + U were $a = b = 5.07$ Å and $c = 13.88$ Å, and they were consistent with the experimental values of $a = 5.04$ Å and $c = 13.75$ Å[67]. Each fully relaxed bulk structure of pristine and Ge-doped α-Fe₂O₃ was used to determine the lattice parameters of each (1×1) slab structure. A vacuum layer at least 12Å was used to minimize the interaction between the periodic surface along z axis. We focused on the surface reaction on (0001) α-Fe₂O₃ surface because it is one of the natural growth faces of hematite[68]. Dopant substitutions were made at both outermost Fe layers to consider the maximum doping effect on surface reactions and to remove the polarization from broken symmetry[54]. Hydrogen passivation was used to prevent the transfer of hydrogen atoms from the active site to the other surface oxygen. We passivated only one of the three surface oxygen atoms to minimize the hydrogen bonding that affects the reaction.

We considered the following OER mechanism with four elementary steps[69].

$$H_2O + * \rightarrow *OH + H^+ + e^- \tag{1}$$

$$*OH \rightarrow *O + H^+ + e^- \tag{2}$$

$$H_2O + *O \rightarrow *OOH + H^+ + e^- \tag{3}$$

$$*OOH \rightarrow * + O_2 + H^+ + e^- \tag{4}$$

The * represents chemisorption with the reactive sites on the surface. According to Rossemiesl et al.[69], at standard conditions (pH = 0, p = 1 bar, T = 298 K), the reaction free energy($\triangle G$) of each step is calculated as follows:

$$\triangle G_A = \Delta E_{*OH} + (\Delta ZPE - T\Delta S)_A - e \cdot \Phi \tag{5}$$

$$\triangle G_B = \Delta E_{*O} - \Delta E_{*OH} + (\Delta ZPE - T\Delta S)_B - e \cdot \Phi \tag{6}$$

$$\triangle G_C = \Delta E_{*OOH} - \Delta E_{*O} + (\Delta ZPE - T\Delta S)_C - e \cdot \Phi \tag{7}$$

$$\triangle G_D = 4.92eV - \Delta E_{*OOH} + (\Delta ZPE - T\Delta S)_D - e \cdot \Phi \tag{8}$$

ΔE_{*OH}, ΔE_{*O} and ΔE_{*OOH} are the binding energies for the adsorption of OH, O, and OOH, respectively. ZPE is the zero-point energy and TΔS is entropic contributions. Φ is the external potential. At the standard condition with $\Phi = 0$, the highest free energy ($\triangle G_{max}$) is equal to reaction potential for electrochemical reaction potential and ($\triangle G_{max} - 1.23$) is equal to overpotential (η).

Data availability
The data that support the findings of this study will be made available upon request.

References
1. Li, J. et al. Plasmon-induced photonic and energy-transfer enhancement of solar water splitting by a hematite nanorod array. *Nat. Commun.* **4**, 2651 (2013).
2. Lin, Y. et al. Hematite-based solar water splitting: challenges and opportunities. *Energy Environ. Sci.* **4**, 4862–4869 (2011).
3. Sivula, K. et al. Photoelectrochemical water splitting with mesoporous hematite prepared by a solution-based colloidal approach. *J. Am. Chem. Soc.* **132**, 7436–7444 (2010).
4. Jang, J.-W. et al. Enabling unassisted solar water splitting by iron oxide and silicon. *Nat. Commun.* **6**, 7447 (2015).
5. Ahn, H. J., Yoon, K. Y., Kwak, M. J. & Jang, J. H. Titanium-doped SiOx passivation layer for greatly enhanced performance of a hematite-based photoelectrochemical system. *Angew. Chem. Int. Ed.* **55**, 9922–9926 (2016).
6. Mao, A., Park, N.-G., Han, G. Y. & Park, J. H. Controlled growth of vertically oriented hematite/Pt composite nanorod arrays: use for photoelectrochemical water splitting. *Nanotechnology* **22**, 175703 (2011).
7. Pendlebury, S. R. et al. Correlating long-lived photogenerated hole populations with photocurrent densities in hematite water oxidation photoanodes. *Energy Environ. Sci.* **5**, 6304–6312 (2012).
8. Wheeler, D. A. et al. Nanostructured hematite: synthesis, characterization, charge carrier dynamics, and photoelectrochemical properties. *Energy Environ. Sci.* **5**, 6682–6702 (2012).
9. Peerakiatkhajohn, P. et al. Stable hematite nanosheet photoanodes for enhanced photoelectrochemical water splitting. *Adv. Mater.* **28**, 6405–6410 (2016).
10. Kim, J. Y. et al. Single-crystalline, wormlike hematite photoanodes for efficient solar water splitting. *Sci. Rep.* **3**, 2681 (2013).
11. Droubay, T. et al. Structure, magnetism, and conductivity in epitaxial Ti-doped α− Fe₂O₃ hematite: experiment and density functional theory calculations. *Phys. Rev. B* **75**, 104412 (2007).
12. Luo, J. et al. Rationally designed hierarchical TiO₂@ Fe₂O₃ hollow nanostructures for improved lithium ion storage. *Adv. Energy Mater.* **3**, 737–743 (2013).

13. Bjoerksten, U., Moser, J. & Graetzel, M. Photoelectrochemical studies on nanocrystalline hematite films. *Chem. Mater.* **6**, 858–863 (1994).

14. Chen, D. et al. Controllable fabrication of mono-dispersed RGO–hematite nanocomposites and their enhanced wave absorption properties. *J. Mater. Chem. A* **1**, 5996–6003 (2013).

15. Barroso, M., Pendlebury, S. R., Cowan, A. J. & Durrant, J. R. Charge carrier trapping, recombination and transfer in hematite (α-Fe₂O₃) water splitting photoanodes. *Chem. Sci.* **4**, 2724–2734 (2013).

16. Le Formal, F. et al. Back electron–hole recombination in hematite photoanodes for water splitting. *J. Am. Chem. Soc.* **136**, 2564–2574 (2014).

17. Segev, G. et al. High solar flux concentration water splitting with hematite (α-Fe2O3) photoanodes. *Adv. Energy Mater.* **6**, 1500817 (2016).

18. Ling, Y., Wang, G., Wheeler, D. A., Zhang, J. Z. & Li, Y. Sn-doped hematite nanostructures for photoelectrochemical water splitting. *Nano Lett.* **11**, 2119–2125 (2011).

19. Hahn, N. T. & Mullins, C. B. Photoelectrochemical performance of nanostructured Ti-and Sn-doped α-Fe₂O₃ photoanodes. *Chem. Mater.* **22**, 6474–6482 (2010).

20. Fu, Z. et al. Surface treatment with Al 3+ on a Ti-doped α-Fe₂O₃ nanorod array photoanode for efficient photoelectrochemical water splitting. *J. Mater. Chem. A* **2**, 13705–13712 (2014).

21. Shen, S. et al. Physical and photoelectrochemical characterization of Ti-doped hematite photoanodes prepared by solution growth. *J. Mater. Chem. A* **1**, 14498–14506 (2013).

22. Cesar, I., Sivula, K., Kay, A., Zboril, R. & Grätzel, M. Influence of feature size, film thickness, and silicon doping on the performance of nanostructured hematite photoanodes for solar water splitting. *J. Phys. Chem. C* **113**, 772–782 (2008).

23. Cesar, I., Kay, A., Gonzalez Martinez, J. A. & Grätzel, M. Translucent thin film Fe₂O₃ photoanodes for efficient water splitting by sunlight: nanostructure-directing effect of Si-doping. *J. Am. Chem. Soc.* **128**, 4582–4583 (2006).

24. Kleiman-Shwarscstein, A., Hu, Y.-S., Forman, A. J., Stucky, G. D. & McFarland, E. W. Electrodeposition of α-Fe₂O₃ doped with Mo or Cr as photoanodes for photocatalytic water splitting. *J. Phys. Chem. C.* **112**, 15900–15907 (2008).

25. Mirbagheri, N. et al. Visible light driven photoelectrochemical water oxidation by Zn-and Ti-doped hematite nanostructures. *ACS Catal.* **4**, 2006–−2015 (2014).

26. Zhou, Z., Long, R. & Prezhdo, O. V. Why silicon doping accelerates electron polaron diffusion in hematite. *J. Am. Chem. Soc.* **141**, 20222–20233 (2019).

27. Park, J. et al. A highly transparent thin film hematite with multi-element dopability for an efficient unassisted water splitting system. *Nano Energy* **76**, 105089 (2020).

28. Zhou, Z. et al. Modulating oxygen vacancies in Sn-doped hematite film grown on silicon microwires for photoelectrochemical water oxidation. *J. Mater. Chem. A* **6**, 15593–15602 (2018).

29. Park, J. W. et al. Improved interfacial charge transfer dynamics and onset shift in nanostructured hematite photoanodes via efficient Ti4+/Sn4+ heterogeneous self-doping through controlled TiO₂ underlayers. *ACS Sustain. Chem. Eng.* **7**, 6947–6958 (2019).

30. Dunn, H. K. et al. Tin doping speeds up hole transfer during light-driven water oxidation at hematite photoanodes. *Phys. Chem. Chem. Phys.* **16**, 24610–−24620 (2014).

31. Yoon, K.-Y. et al. A selectively decorated Ti-FeOOH co-catalyst for a highly efficient porous hematite-based water splitting system. *J. Mater. Chem. A* **4**, 18730–18736 (2016).

32. Li, M. et al. Boosting the photoelectrochemical water oxidation at hematite photoanode by innovating a hierarchical ball-on-wire-array structure. *ACS Appl. Energy Mater.* **1**, 5836–5841 (2018).

33. Tang, S. et al. 3D hierarchical nanorod@ nanobowl array photoanode with a tunable light-trapping cutoff and bottom-selective field enhancement for efficient solar water splitting. *Small* **15**, 1804976 (2019).

34. Zhang, Z. et al. Interfacial oxygen vacancies yielding long-lived holes in hematite mesocrystal-based photoanodes. *Nat. Commun.* **10**, 1–12 (2019).

35. Zhang, P. et al. Oriented Ti doped hematite thin film as active photoanodes synthesized by facile APCVD. *Energy Environ. Sci.* **4**, 1020–1028 (2011).

36. Wang, Z. L. et al. Synergetic effect of conjugated Ni(OH)(2)/IrO2 cocatalyst on titanium-doped hematite photoanode for solar water splitting. *J. Phys. Chem. C* **119**, 19607–19612 (2015).

37. Zhou, Z., Huo, P., Guo, L. & Prezhdo, O. V. Understanding hematite doping with group IV elements: a DFT+ U study. *J. Phys. Chem. C* **119**, 26303–26310 (2015).

38. Shen, S. et al. Effect of Cr doping on the photoelectrochemical performance of hematite nanorod photoanodes. *Nano Energy* **1**, 732–741 (2012).

39. Liao, P., Toroker, M. C. & Carter, E. A. Electron transport in pure and doped hematite. *Nano Lett.* **11**, 1775–1781 (2011).

40. Liu, J. et al. Highly oriented Ge-doped hematite nanosheet arrays for photoelectrochemical water oxidation. *Nano Energy* **9**, 282–290 (2014).

41. Liu, J. et al. Ge-doped hematite nanosheets with tunable doping level, structure and improved photoelectrochemical performance. *Nano Energy* **2**, 328–336 (2013).

42. Li, M. et al. Morphology and doping engineering of Sn-doped hematite nanowire photoanodes. *Nano Lett.* **17**, 2490–2495 (2017).

43. Annamalai, A. et al. Activation of hematite photoanodes for solar water splitting: effect of FTO deformation. *J. Phys. Chem. C* **119**, 3810–3817 (2015).

44. Zandi, O. & Hamann, T. W. Enhanced water splitting efficiency through selective surface state removal. *J. Phys. Chem. Lett.* **5**, 1522–1526 (2014).

45. Zhao, L. et al. Enhanced efficiency of hematite photoanode for water splitting with the doping of Ge. *Int. J. Hydrog. Energy* **43**, 12646–12652 (2018).

46. Li, C. et al. Surviving high-temperature calcination: ZrO₂-induced hematite nanotubes for photoelectrochemical water oxidation. *Angew. Chem. Int. Ed.* **56**, 4150–4155 (2017).

47. Zhao, X. et al. New insight into the roles of oxygen vacancies in hematite for solar water splitting. *Phys. Chem. Chem. Phys.* **19**, 1074–1082 (2017).

48. Ahn, H. J., Yoon, K. Y., Kwak, M. J., Park, J. & Jang, J. H. Boron doping of metal-doped hematite for reduced surface recombination in water splitting. *ACS Catal.* **8**, 11932–11939 (2018).

49. Pu, A. et al. Coupling Ti-doping and oxygen vacancies in hematite nanostructures for solar water oxidation with high efficiency. *J. Mater. Chem. A* **2**, 2491–2497 (2014).

50. Wang, Z. et al. Understanding the roles of oxygen vacancies in hematite-based photoelectrochemical processes. *Angew. Chem. Int. Ed.* **58**, 1030–1034 (2019).

51. Zardetto, V., Brown, T. M., Reale, A. & Di Carlo, A. Substrates for flexible electronics: a practical investigation on the electrical, film flexibility, optical, temperature, and solvent resistance properties. *J. Polym. Sci. B. Polym. Phys.* **49**, 638–648 (2011).

52. Sung, J. C. & Lu, C. H. Effects of sputtering conditions on the photovoltaic properties of Al-doped zinc oxide films for Cu(In,Ga)Se-2 thin-film solar cells. *J. Mater. Sci: Mater. Electron.* **28**, 15442–15450 (2017).

53. Iandolo, B. et al. Correlating flat band and onset potentials for solar water splitting on model hematite photoanodes. *RSC Adv.* **5**, 61021–61030 (2015).

54. Liao, P., Keith, J. A. & Carter, E. A. Water oxidation on pure and doped hematite (0001) surfaces: Prediction of Co and Ni as effective dopants for electrocatalysis. *J. Am. Chem. Soc.* **134**, 13296–13309 (2012).

55. Hufnagel, A. G. et al. Why tin-doping enhances the efficiency of hematite photoanodes for water splitting—the full picture. *Adv. Funct. Mater.* **28**, 1804472 (2018).

56. Zhang, X., Klaver, P., van Santen, R., Van De Sanden, M. & Bieberle-Hütter, A. Oxygen evolution at hematite surfaces: the impact of structure and oxygen vacancies on lowering the overpotential. *J. Phys. Chem. C* **120**, 18201–18208 (2016).

57. Roy, S. & Botte, G. G. Perovskite solar cell for photocatalytic water splitting with a TiO₂/Co-doped hematite electron transport bilayer. *RSC Adv.* **8**, 5388–5394 (2018).

58. Morales-Guio, C. G. et al. An optically transparent iron nickel oxide catalyst for solar water splitting. *J. Am. Chem. Soc.* **137**, 9927–9936 (2015).

59. Sabba, D. et al. Perovskite–hematite tandem cells for efficient overall solar driven water splitting. *Nano Lett.* **15**, 3833–3839 (2015).

60. Gurudayal et al. Atomically altered hematite for highly efficient perovskite tandem water-splitting devices. *ChemSusChem* **10**, 2449–−2456 (2017).

61. Urbain, F. et al. Multilayered hematite nanowires with thin-film silicon photovoltaics in an all-earth-abundant hybrid tandem device for solar water splitting. *ChemSusChem* **12**, 1428–1436 (2019).

62. Jeon, N. J. et al. Compositional engineering of perovskite materials for high-performance solar cells. *Nature* **517**, 476 (2015).

63. Kresse, G. & Joubert, D. From ultrasoft pseudopotentials to the projector augmented-wave method. *Phys. Rev. B* **59**, 1758 (1999).

64. Kresse, G. & Furthmüller, J. Efficient iterative schemes for ab initio total-energy calculations using a plane-wave basis set. *Phys. Rev. B* **54**, 11169 (1996).

65. Perdew, J. P., Burke, K. & Ernzerhof, M. Generalized gradient approximation made simple. *Phys. Rev. Lett.* **77**, 3865 (1996).

66. Wang, L., Maxisch, T. & Ceder, G. Oxidation energies of transition metal oxides within the GGA+ U framework. *Phys. Rev. B* **73**, 195107 (2006).

67. Finger, L. W. & Hazen, R. M. Crystal structure and isothermal compression of Fe₂O₃, Cr₂O₃, and V₂O₃ to 50 kbars. *J. Appl. Phys.* **51**, 5362–5367 (1980).

68. Lad, R. J. & Henrich, V. E. Structure of α-Fe₂O₃ single crystal surfaces following Ar + ion bombardment and annealing in O₂. *Surf. Sci.* **193**, 81–93 (1988).

69. Rossmeisl, J., Qu, Z.-W., Zhu, H., Kroes, G.-J. & Nørskov, J. K. Electrolysis of water on oxide surfaces. *J. Electroanal. Chem.* **607**, 83–89 (2007).

Acknowledgements

Author contributions

K.-Y.Y. conceived the idea and designed experiments; J.-H.J. supervised the project; K.-Y.Y. and J.P fabricated the photoanodes and conducted electrochemical analyses; M.J. and S.-G.J. fabricated the perovskite solar cell and checked the efficiency; S.I.S. confirmed the results of the solar cell; H.S.L. and J.H.S. conducted DFT calculations; J.H.L. confirmed the calcualtion results; J.P. and M.-J.K. performed SEM, XRD, Raman and EXAFS characterizations; All authors discussed the results and co-wrote the manuscript.

Competing interests

The authors declare no competing interests.

Additional information

Supplementary information The online version contains supplementary material available at https://doi.org/10.1038/s41467-021-24428-7.

Correspondence and requests for materials should be addressed to J.-H.J.

Peer review information *Nature communications* thanks Laia Francàs and other, anonymous, reviewers for their contributions to the peer review of this work.

Publisher's note Springer Nature remains neutral with regard to jurisdictional claims in published maps and institutional affiliations.